



ELSEVIER

Contents lists available at ScienceDirect

Mechanism and Machine Theory

journal homepage: www.elsevier.com/locate/mechmt

Research paper

Stiffness evaluation of a novel ankle rehabilitation exoskeleton with a type-variable constraint

Tun Wang^{a,b}, Yen-Hua Lin^b, Emmanouil Spyarakos-Papastavridis^b, Sheng Quan Xie^c, Jian S. Dai^{a,b,*}^a Shenzhen Key Laboratory of Biomimetic Robotics and Intelligent Systems, Southern University of Science and Technology, Shenzhen, 518055, China^b Centre for Robotics Research, Faculty of Natural, Mathematical & Engineering Sciences, King's College London, London, WC2R 2LS, UK^c School of Electrical and Electronic Engineering, University of Leeds, LS2 9JT, UK

ARTICLE INFO

Keywords:

Ankle rehabilitation exoskeleton
Stiffness analysis
Type-variable constraint
Transition configurations

ABSTRACT

This paper presents a novel ankle rehabilitation exoskeleton with two rotational degrees of freedom, which is suitable for dynamical rehabilitation for patients with neurological impairments. Its stiffness performance is assessed in consideration that the interaction between the footplate and the ground may deflect the mechanism away from the desired/predefined motion patterns. The novel design employs a universal-prismatic-universal (U-P-U) joint link, whose constraint type changes between a couple and a line vector during manipulation of the exoskeleton. To conduct a stiffness analysis of such a mechanism with a type-variable constraint – for the first time – a modified screw-based method (SBM) is proposed. Comparisons with the results obtained from finite element analysis verified that, the modified SBM provides reliable estimates of the exoskeleton's stiffness within the complete workspace (covering the constraint-type transition configurations). The stiffness of the exoskeleton is further evaluated by acquiring the minimum/maximum stiffness values, after computing the distribution of the most crucial linear and angular stiffness parameters within the workspace. Moreover, the influence of the architectural parameters on the stiffness properties is considered for further design optimization.

1. Introduction

1.1. Ankle rehabilitation devices

People who suffer from neurological impairments, such as stroke and spinal cord injuries, usually have severe motor dysfunction, which considerably compromises their locomotion [1]. As one of the major weight-bearing structures, the ankle-foot complex plays an important role during ambulation [2]. To regain their walking ability, patients have to undertake physical therapy to augment the strength and endurance of the muscle/s and ligament/s around the ankle joint, and to stimulate the ankle-foot complex's motor functions. The ankle-foot complex possesses a sophisticated musculoskeletal structure, which enables it to realize three rotations about the axes passing through the complex centre, i.e. inversion/eversion (I/E), dorsi-/plantarflexion (D/P) and adduction/abduction

* Corresponding author.

E-mail addresses: jian.dai@kcl.ac.uk, daijs@sustech.edu.cn (J.S. Dai).<https://doi.org/10.1016/j.mechmachtheory.2022.105071>

Received 12 June 2022; Received in revised form 30 July 2022; Accepted 16 August 2022

Available online 3 October 2022

0094-114X/© 2022 The Author(s).

Published by Elsevier Ltd. This is an open access article under the CC BY license (<http://creativecommons.org/licenses/by/4.0/>).

Published by Elsevier Ltd. This is an open access article under the CC BY license

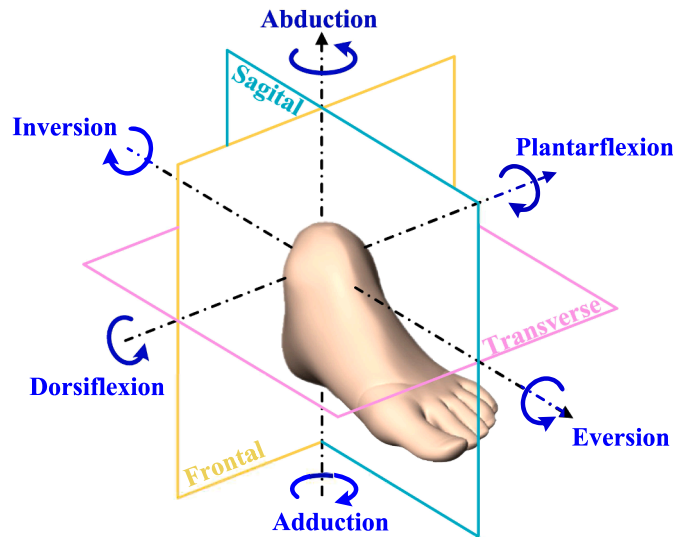


Fig. 1. Rotations of ankle-foot complex.

(A/A). As shown in Fig. 1, the three motions occur in the frontal, sagittal, and transverse planes, respectively. At the clinic, the complex is manually guided by the physiotherapist to perform extensive and repetitive training within the prescribed range of motion (ROM) of the three degrees of freedom (DOFs). Compared to the aforementioned, conventional rehabilitation therapies, robot-assisted rehabilitation solutions possess significant benefits in terms of providing scientifically motivated, quantifiable, and automated exercises. In general, the designed systems can be classified into two categories: stationary mechanisms and wearable devices (exoskeletons/active orthosis devices) [3,4]. The former assist patients with the realisation of exercises that do not entail locomotion, and aim to help them gradually recover the ankle-foot complex's ROM and improve balance/proprioception. The latter are developed for dynamical rehabilitation, as they aim to help control the complex's position during ambulation, and to then recover a normal walking gait [5].

Stationary systems have been developed for more than 20 years, starting from 1999 [6,7]. The majority of designs produced during the first 10 years [8–11] overlooked a very important design criterion, i.e. ensuring that the rotational centre of the mechanism matched that of the ankle-foot complex, despite the fact that misalignment of the two centres may lead to discomfort, pain or even secondary injury to the biological joint [12]. Tsoi et al. [13] described construction of a 4 U-P-S (universal-prismatic-spherical joint) parallel device actuating the platform from above, which solves the misalignment problem but may give rise to safety issues. In subsequent years, other scholars [14–17] proposed various mechanisms with remote centres-of-motion (RCMs) [18] to realize the same function; in their research studies, the complex is regarded as a fixed rotational centre. Nevertheless, these mechanisms require manual adjustments to match the ankle complex centres. Unlike stationary systems that are required to realise exercises for all three rotation DOFs, wearable robots mainly actively assist D/P and I/E motions, although they neglect (or passively support) A/A motion due to its marginal contribution in terms of restoring a normal walking gait [19,20]. Also, the majority of these kinds of devices employ serial mechanisms as their main structure. Nevertheless, owing to the inherent advantages of parallel manipulators, such as high stiffness, lower inertia, and large payload capacity, they are employed by some researchers to construct wearable systems. Typical examples are the prototypes demonstrated in [12,19,21], which share a common feature: they integrate the human leg as part of the designed mechanism. Amongst them, only the Anklebot presented in [19] can match the complex centre when performing walking exercises. However, this robot lacks a decoupled-control capacity, and to some extent, accurate position control relies on the coordinated motion of the two equipped linear actuators.

Based on the above, Wang et al. [22] proposed a novel 2-DOF ankle rehabilitation exoskeleton in a parallel architecture for gait rehabilitation, which was later developed into a reconfigurable mechanism capable of providing both static and dynamic rehabilitation modes [23]. Analysis results reveal that, in every possible configuration, this 2-DOF exoskeleton can always match the ankle-foot complex centre no matter how the latter moves, and the matching property is automatically realised once the patient wears this device. Moreover, compared to the existing parallel rehabilitation systems for gait exercises, another prominent feature of this design is that it can realise decoupled control once the links are arranged in a specific manner. In this paper, the performance of this novel exoskeleton design is further evaluated in terms of its passive stiffness.

1.2. Stiffness analysis approaches

A mechanism's stiffness indicates the magnitudes of the end-effector displacements resulting from the deformations of the mechanism's components, under the effect of external torques or forces [24], and it has a direct impact on the manipulator's positional/orientational accuracy. When the designed exoskeleton performs dynamical rehabilitation exercises, the propulsion is generated from the interaction between the sole and the ground. These external wrenches may compel the footplate to be deflected away

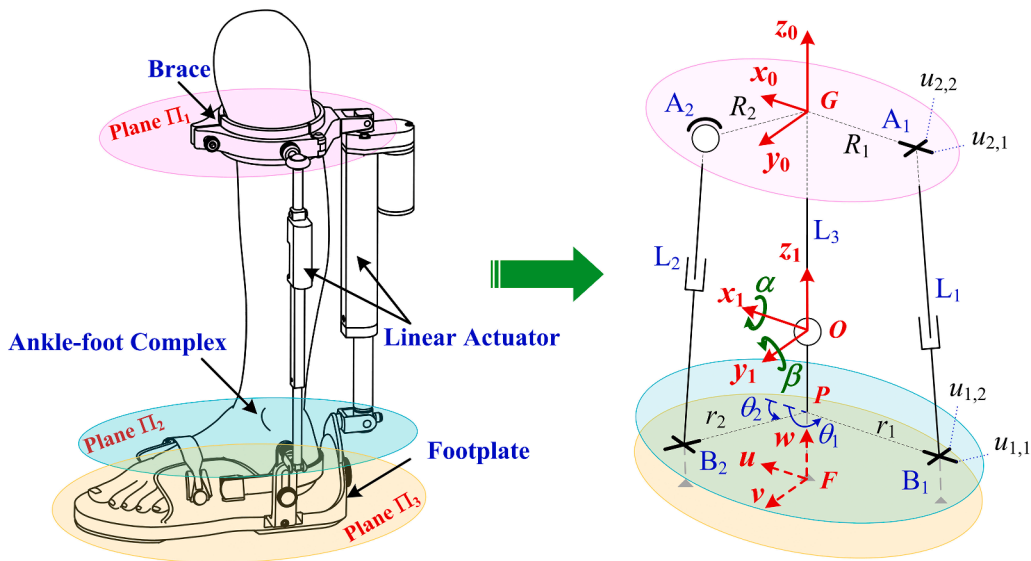


Fig. 2. Design of the novel ankle rehabilitation exoskeleton and its geometry in the initial configuration.

from its desired orientations/predefined motion patterns, and further affect rehabilitation performance [15,25,26]. Hence, it is of pivotal importance to assess the rehabilitation exoskeleton’s stiffness, and gain a clear understanding on strategies to improve the design

There are various methods for evaluating a parallel mechanism’s stiffness. Amongst them, finite element analysis (FEA) is well developed and offers the highest accuracy [27]. However, this method is not analytical and always requires a rebuilding of the model when the parallel mechanism’s configuration is changed, which is labour-intensive and time-consuming. Due to its considerable computational requirements, FEA is typically used at the verification stage or as an assistive measure in evaluating the stiffness parameters of the mechanism parts that are difficult to simplify. In contrast, the matrix structural analysis (MSA) approach possesses the advantage of reduced computational effort, and can even produce analytical stiffness matrices in some cases [28]. However, this technique necessitates a trade-off between accuracy and computational time, and the stiffness modelling may be inaccurate when simplifying structures with complex cross sections, or shapes, in an inappropriate way. Besides, it needs to deal with rather high-dimensional matrix operations, and this to some extent impinges on its widespread applicability. Another commonly used approach is known as the virtual joint method (VJM) (also referred to as “lumped modelling”), which can provide acceptable accuracy with lower computational effort [29]. This approach stemmed from Gosselin’s research [30], in which only the actuators’ compliance was taken into account and simplified as one-dimensional linear springs. Then the VJM was further improved by integrating the flexibility of the links, which were presented as rigid beams supplemented by linear or torsional springs [31]. The research described in [32] suggests using m -DOF springs to better describe the deformation of components linked by (6- m) DOF passive joints. To date, this method has a number of variations, differing in modelling assumptions, numerical techniques, and combined theories, which can be exploited in analytical parametric analysis of both over-constrained and non-over-constrained parallel mechanisms. Considering the convenience offered by screw theory in terms of constructing the Jacobian matrix, especially the overall Jacobian matrix of parallel mechanisms with less than 6 DOFs (i.e. limited-DOF parallel mechanisms) [33], it is also usually employed to assist with stiffness modelling [24,34–39]. This screw-based method (SBM) [40,41] provides an intuitive means of deriving the overall stiffness matrix, which is able to explicitly describe the compliances in the presence of both actuation, and constraint, forces.

In addition, the parallel mechanisms presented in the existing publications are always subjected to type-invariant constraints. Considering the U-P-U (or its function-equivalent arrangement) link that is employed in the construction of the exoskeleton introduced in this paper, for instance: although it is frequently used in various designs, the U joints’ axes are always set as parallel [34,42] or arranged to have large intersection angles [27,43]. Accordingly, in these designs, the constraint of this U-P-U link to the moving platform is a Cartesian torque or force within the overall workspace. However, during manipulation of the proposed exoskeleton, the constraint type of the U-P-U link may change between torque and force, and there are few stiffness-analysis-orientated treatises discussing this kind of situation. Meanwhile, it has been found that, although the conventional SBM possesses the aforementioned, desirable features, it may only be suitable for the two forenamed cases with type-invariant constraints, and may not be directly applicable to situations where constraint-type transitions are bound to occur, i.e. the circumstances discussed in this paper.

Hence, a modified SBM is presented in this paper, and based on this method a stiffness evaluation of the mechanism with a type-variable constraint is introduced for the first time. Specifically, this paper is organized as follows: Section 2 provides a brief introduction of the geometry and motion features of the proposed novel exoskeleton; Section 3 details the identification of the stiffness model of the mechanism via conventional SBM; Section 4 presents the modified SBM and corresponding numerical verification once the workspace has been determined, based on which the exoskeleton’s stiffness properties are explored. Also, the most effective way to improve the design’s stiffness performance is revealed. Finally, the concluding remarks are presented in Section 5.

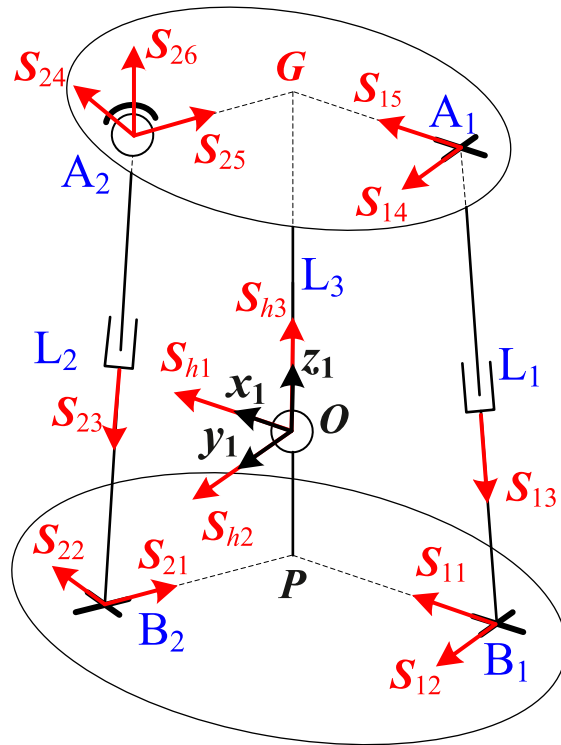


Fig. 3. Screws in $L_1 \sim L_3$ link.

2. Geometric modelling of the novel ankle rehabilitation exoskeleton

Fig. 2 displays the designed exoskeleton (worn on a patient’s left leg) and the corresponding geometrical drawing. It consists of a brace fixed around the human shank, a footplate used to accommodate the human foot, a rear link (L_1) in a U-P-U configuration, and a lateral link (L_2) in an S-P-U configuration. When worn by the patient, their leg will behave as the central strut (L_3) of this mechanism. Following a frequently used approach of modelling the ankle-foot complex, the complex is reduced to a spherical joint (denoted by O) in the design. A_i ($i = 1, 2$) denote the connection points of the two linear actuators to the brace. The two points, together with the centre of brace, G , are located in Plane Π_1 . The two links connect to the footplate (Plane Π_3) via B_i , which are located in the Π_2 plane, parallelly offsetting the Π_3 plane. Two fixed coordinate systems, (x_0, y_0, z_0) and (x_1, y_1, z_1) , are respectively built at G and O , with coordinate axes parallel to each other. OP and OF denote the vertical distance from the ankle to Π_2 and Π_3 in the initial configuration, where the brace and footplate are parallel to each other. The $GO=h_0$, $OP=h_1$, $OF=h_f$ expressions are defined for notational convenience. A moving reference frame, whose position is changing with the rotation of the footplate, is attached to F , with its axes always parallel to those of frame G . The two actuated links’ topology can be solely determined by θ_b , which is the angle between the positive direction of the x_0 axis, and the $A_i B_i$ plane. The relative locations of A_i and B_i , with respect to the plane centres, are described by R_i and r_b , respectively. Since the Π_2 and Π_3 planes are rigidly connected and will therefore possess the same orientations, the Π_3 plane will hereafter be omitted from any illustrations, for the purpose of conciseness.

Moreover, the arrangements of the universal joints in L_1 need to meet the following geometric conditions for realising the anticipated function. In the initial configuration, the $u_{1,1}$ axis is parallel to the $u_{2,1}$ axis, and the two axes respectively point to P and G . In the meantime, the $u_{1,2}$ and $u_{2,2}$ axes should be parallel to each other, and perpendicular to line $A_1 B_1$ in any configuration. Also, since Link L_2 imposes no constraints on the footplate, the directions of the universal joints in this link have no special geometric restraints.

By means of screw theory, the motion features of the mechanism can be derived (here, only the conclusions are presented and more details can be referred to in [22]). The exoskeleton has two rotational DOFs and the two rotational axes always pass through the ankle complex centre, O . One axis is the line connecting O and the intersection point of $u_{1,1}$ and $u_{2,1}$ (this axis turns into the x_1 axis when $u_{1,1}$ and $u_{2,1}$ are parallel), and the other axis is the normal of the $A_1 B_1 O G$ plane passing through O .

3. Stiffness modelling

3.1. Derivation of overall Jacobian matrix

According to [44], the twist of the footplate of the exoskeleton can be defined as $T_M = [\omega^T \ v^T]^T$, in which ω is the angular velocity of the footplate, and v is the linear velocity of point F . Fig. 3 displays the unit screws associated with the joints in the three links. In this

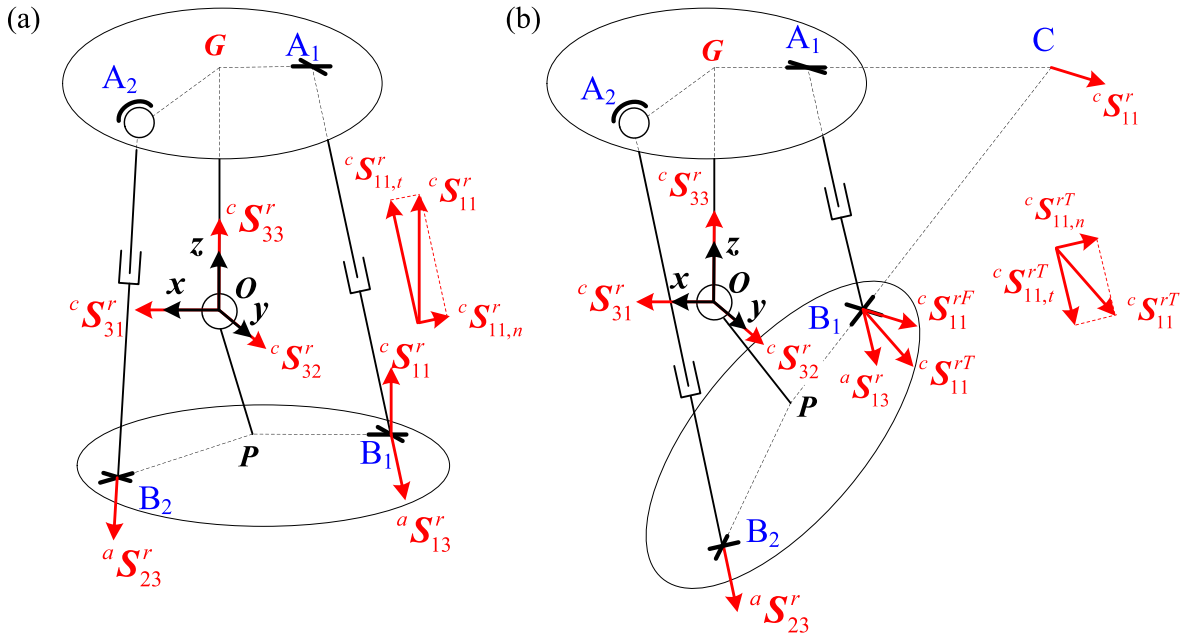


Fig. 4. Reciprocal screws in (a) Case I and (b) Case II.

figure, the spherical joint is modelled as three intersecting, non-coplanar revolute joints, and the universal joint is equivalent to two intersecting revolute joints. Then, the instantaneous twist of the footplate can be expressed as

$$T_M = \sum_{j=1}^{C_i} \dot{q}_{ij} S_{ij}, \quad i = 1, 2, 3, \tag{1}$$

where, S_{ij} denotes the unit screw of the j th joint of the i th link, and \dot{q}_{ij} is the corresponding joint rate. C_i is the connectivity of the i th link, which is defined as the DOFs associated with all the joints of this link. Hence, the connectivity of the $L_1 \sim L_3$ links is 5, 6 and 3, respectively. Computing (1) for each one of these three links produces

$$T_M = \dot{\theta}_{11} S_{11} + \dot{\theta}_{12} S_{12} + \dot{\theta}_{13} S_{13} + \dot{\theta}_{14} S_{14} + \dot{\theta}_{15} S_{15}, \tag{2}$$

$$T_M = \dot{\theta}_{21} S_{21} + \dot{\theta}_{22} S_{22} + \dot{\theta}_{23} S_{23} + \dot{\theta}_{24} S_{24} + \dot{\theta}_{25} S_{25} + \dot{\theta}_{26} S_{26}, \tag{3}$$

$$T_M = \dot{\theta}_{31} S_{31} + \dot{\theta}_{32} S_{32} + \dot{\theta}_{33} S_{33}. \tag{4}$$

Denote $\mathbf{b}_i = \mathbf{F}B_i$, $\mathbf{l}_i = \mathbf{A}_i B_i$ ($i = 1, 2$) and $\mathbf{h} = \mathbf{F}O$, the expressions of the above screws in the F frame (which is not shown in Fig. 3) are the following

$$S_{11} = \begin{bmatrix} s_{11} \\ \mathbf{b}_1 \times s_{11} \end{bmatrix}, S_{12} = \begin{bmatrix} s_{12} \\ \mathbf{b}_1 \times s_{12} \end{bmatrix}, S_{13} = \begin{bmatrix} \mathbf{0} \\ s_{13} \end{bmatrix}, S_{14} = \begin{bmatrix} s_{14} \\ (\mathbf{b}_1 - \mathbf{l}_1) \times s_{14} \end{bmatrix}, S_{15} = \begin{bmatrix} s_{15} \\ (\mathbf{b}_1 - \mathbf{l}_1) \times s_{15} \end{bmatrix}, \tag{5}$$

$$S_{21} = \begin{bmatrix} s_{21} \\ \mathbf{b}_2 \times s_{21} \end{bmatrix}, S_{22} = \begin{bmatrix} s_{22} \\ \mathbf{b}_2 \times s_{22} \end{bmatrix}, S_{23} = \begin{bmatrix} \mathbf{0} \\ s_{23} \end{bmatrix}, S_{24} = \begin{bmatrix} s_{24} \\ (\mathbf{b}_2 - \mathbf{l}_2) \times s_{24} \end{bmatrix}, S_{25} = \begin{bmatrix} s_{25} \\ (\mathbf{b}_2 - \mathbf{l}_2) \times s_{25} \end{bmatrix}, S_{26} = \begin{bmatrix} s_{26} \\ (\mathbf{b}_2 - \mathbf{l}_2) \times s_{26} \end{bmatrix}, \tag{6}$$

$$S_{31} = \begin{bmatrix} s_{31} \\ \mathbf{h} \times s_{31} \end{bmatrix}, S_{32} = \begin{bmatrix} s_{32} \\ \mathbf{h} \times s_{32} \end{bmatrix}, S_{33} = \begin{bmatrix} s_{33} \\ \mathbf{h} \times s_{33} \end{bmatrix}. \tag{7}$$

The screws that are reciprocal to all the joint screws of the i th link are defined as the reciprocal screws of constraints – they form a $(6 - C_i)$ reciprocal screw system [45]. Letting ${}^c S_{ij}$ denote the j th reciprocal screw of the i th link expressed in ray coordinates, and taking the orthogonal product of both sides of (1) with each reciprocal screw, yields

$$\left(\Delta^c S_{ij}^r \right)^T T_M = 0, \tag{8}$$

in which,

$$\Delta = \begin{bmatrix} \mathbf{0} & \mathbf{I} \\ \mathbf{I} & \mathbf{0} \end{bmatrix}_{6 \times 6}.$$

The swap operator, Δ , interchanges the first and last three components of a screw; $\mathbf{0}$ and \mathbf{I} represent 3×3 zero, and identity, matrices, respectively.

Since $C_2=6$, the L_2 link has no reciprocal screws of constraints, and L_3 has three reciprocal screws passing through point O. The expressions of the three screws are displayed in (9), which represent three forces.

$${}^cS_{31}^r = \begin{bmatrix} s_{31} \\ \mathbf{h} \times s_{31} \end{bmatrix}, {}^cS_{32}^r = \begin{bmatrix} s_{32} \\ \mathbf{h} \times s_{32} \end{bmatrix}, {}^cS_{33}^r = \begin{bmatrix} s_{33} \\ \mathbf{h} \times s_{33} \end{bmatrix}. \tag{9}$$

Link L_1 has only one reciprocal screw, and this screw may represent a torque or a force depending on the specific, instantaneous configuration of the exoskeleton. Correspondingly, two different cases are defined in this paper. Case I represents the exoskeleton configurations for which the s_{11}/s_{15} and s_{12}/s_{14} relations hold. According to [22], the reciprocal screw of L_1 in this case, is a torque whose direction is parallel to the $(s_{11} \times s_{12})$ vector, and can be expressed using (10). In this equation, this reciprocal screw is further decoupled into two couples with directions along, and perpendicular to, L_1 , respectively; these are illustrated in Fig. 4(a).

$${}^cS_{11}^r = \begin{bmatrix} \mathbf{0} \\ s_{11} \times s_{12} \end{bmatrix} = {}^cS_{11,t}^r + {}^cS_{11,n}^r = \begin{bmatrix} \mathbf{0} \\ -p_{n1}s_{13} \end{bmatrix} + \begin{bmatrix} \mathbf{0} \\ p_{n1}(s_{12} \times s_{13}) \end{bmatrix}. \tag{10}$$

In the above equation, $p_{n1} = \|s_{13} \cdot (s_{11} \times s_{12})\|$, $p_{t1} = \sqrt{1 - p_{n1}^2}$.

Contrarily, Case II refers to the other exoskeleton configurations where s_{12}/s_{14} , but s_{11} and s_{15} intersect. In these, the reciprocal screw of L_1 will represent a pure force passing through the intersection point C and perpendicular to the A_1B_1C plane. Fig. 4(b) displays an arbitrary configuration corresponding to Case II, whose reciprocal screw can be expressed as

$${}^cS_{11}^r = \begin{bmatrix} s_{12} \\ \mathbf{r}_C \times s_{12} \end{bmatrix}, \tag{11}$$

where,

$$s_{12} = s_{14} = \frac{s_{11} \times s_{13}}{\|s_{11} \times s_{13}\|}, \mathbf{r}_C = FC.$$

This reciprocal screw can be equivalently decoupled into a force passing through B_1 and a torque with direction parallel to $s_{12} \times s_{11}$ [46]. Meanwhile, similar to Case I, the torque can be further divided into two parts, as displayed in (12) below:

$${}^cS_{11}^r = {}^cS_{11}^{rf} + {}^cS_{11}^{rt} = \begin{bmatrix} s_{12} \\ \mathbf{b}_1 \times s_{12} \end{bmatrix} + \begin{bmatrix} \mathbf{0} \\ (\mathbf{r}_C - \mathbf{b}_1) \times s_{12} \end{bmatrix} = {}^cS_{11}^{rf} + {}^cS_{11,t}^{rt} + {}^cS_{11,n}^{rt} = \begin{bmatrix} s_{12} \\ \mathbf{b}_1 \times s_{12} \end{bmatrix} + \begin{bmatrix} \mathbf{0} \\ p_{t2} \times s_{13} \end{bmatrix} + \begin{bmatrix} \mathbf{0} \\ p_{n2}(s_{12} \times s_{13}) \end{bmatrix}, \tag{12}$$

in which, $p_{t2} = \|s_{13} \cdot ((\mathbf{r}_C - \mathbf{b}_1) \times s_{12})\|$, $p_{n2} = \|(s_{12} \times s_{13}) \cdot ((\mathbf{r}_C - \mathbf{b}_1) \times s_{12})\|$.

The reciprocal screws of constraints for L_1 and L_3 can be arranged into matrix form as

$$\mathbf{J}_c \mathbf{T}_M = \dot{\mathbf{q}}_c, \tag{13}$$

\mathbf{J}_c is defined as the generalized Jacobian of constraints [37]. \mathbf{J}_c possesses two different expressions, corresponding to the two distinct cases, as shown below:

$$\mathbf{J}_{c1} = \begin{pmatrix} (\mathbf{h} \times s_{31})^T & s_{31}^T \\ (\mathbf{h} \times s_{32})^T & s_{32}^T \\ (\mathbf{h} \times s_{33})^T & s_{33}^T \\ -p_{n1}s_{13}^T & \mathbf{0}^T \\ p_{n1}(s_{12} \times s_{13})^T & \mathbf{0}^T \end{pmatrix}_{5 \times 6}, \mathbf{J}_{c2} = \begin{pmatrix} (\mathbf{h} \times s_{31})^T & s_{31}^T \\ (\mathbf{h} \times s_{32})^T & s_{32}^T \\ (\mathbf{h} \times s_{33})^T & s_{33}^T \\ (\mathbf{b}_1 \times s_{12})^T & s_{12}^T \\ p_{t2}s_{13}^T & \mathbf{0}^T \\ p_{n2}(s_{12} \times s_{13})^T & \mathbf{0}^T \end{pmatrix}_{6 \times 6}. \tag{14}$$

If the link actuators are locked, additional basis screws appear; these basis screws – which do not belong to \mathbf{J}_c – are reciprocal to all the passive joint screws of each link. Each one of these represents the reciprocal screw of actuation. If the k th joint of the i th link is actuated, the reciprocal screw of actuation can be represented by ${}^aS_{ik}$, and satisfies the following relationship:

$$(\Delta^a S_{ik}^r)^T \mathbf{T}_M = \dot{\mathbf{q}}_{ik} (\Delta^a S_{ik}^r)^T S_{ik} \tag{15}$$

For the exoskeleton design under consideration, L_1 and L_2 are the drive links whose actuation forces are generated solely via prismatic joints; hence, the reciprocal screws for the L_1 and L_2 links, respectively, are

$${}^aS_{13}^r = \begin{bmatrix} s_{13} \\ \mathbf{b}_1 \times s_{13} \end{bmatrix}, {}^aS_{23}^r = \begin{bmatrix} s_{23} \\ \mathbf{b}_2 \times s_{23} \end{bmatrix}. \tag{16}$$

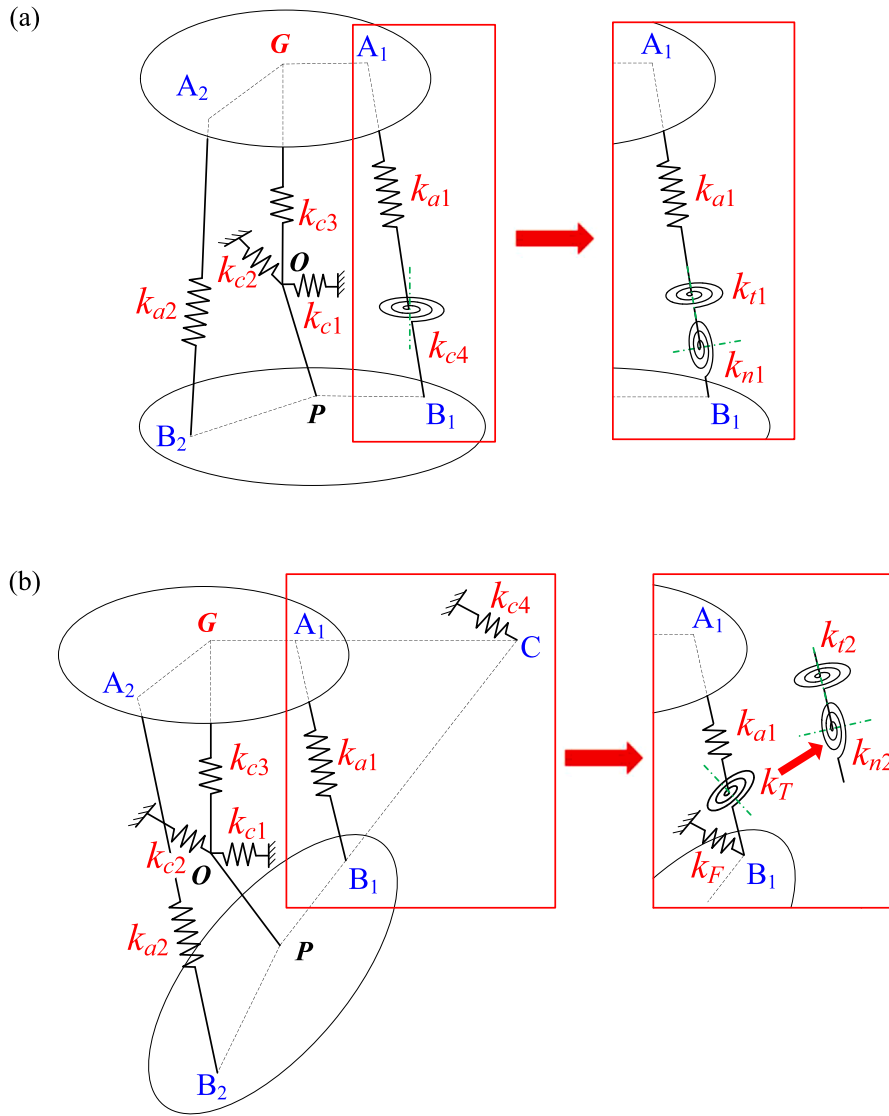


Fig. 5. Stiffness equivalent model of the exoskeleton in (a) Case I and (b) Case II. Green dash-dotted lines represent the directions of rotational springs.

These constitutes pure forces pointing along A_iB_i and passing through the centre of the lower U-joint of each link. Arranging them into matrix form yields

$$J_a T_M = \dot{q}_a, \tag{17}$$

in which,

$$J_a = \begin{pmatrix} (b_1 \times s_{13})^T & s_{13}^T \\ (b_2 \times s_{23})^T & s_{23}^T \end{pmatrix}, \dot{q}_a = \begin{pmatrix} \dot{d}_{13} \\ \dot{d}_{23} \end{pmatrix}.$$

J_a is termed the Jacobian of actuations. Then, the overall Jacobian matrix, J , can be acquired by assembling J_a and J_c , as follows

$$J = \begin{pmatrix} J_a \\ J_c \end{pmatrix}. \tag{18}$$

3.2. Stiffness matrix determination

As was previously described, when the patient wears the exoskeleton, the human shank acts as one of its links. The musculoskeletal

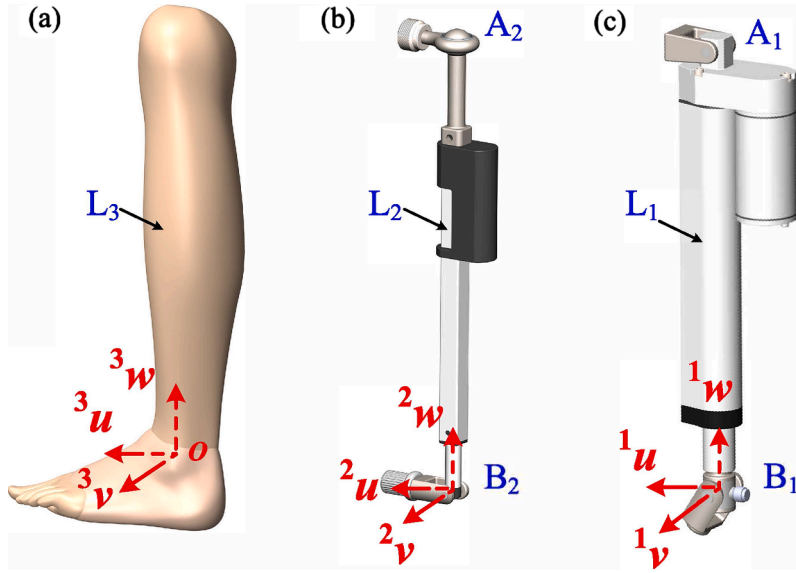


Fig. 6. Local frames in three links.

system of the human shank is relatively complex, as it comprises bones, muscles, tendons, skin, tissues, etc. For the sake of simplicity, it is modelled as an isotropic elastic material with uniform density [47] in the simulation. Since the links' deformations are non-negligible, their stiffnesses are considered to be the main source of the parallel mechanism's stiffness. This assumption also paves the way for potential replacement of the existing drives with more compliant, linear actuation units, e.g. series elastic actuators (SEA) [48], in the future optimization. In comparison with the tradition metallic actuators, SEA possesses a light weight and low inertia [12]. This kind of unit may also provide the exoskeleton with high-fidelity force control and active back-driveability, while ensuring safety, robustness and force-mitigation during the post-impact phase [49–53]. In addition, another assumption is made in this paper, i.e. gravitational effects are neglected. Based on the above, the stiffness model can be built in the manner described in the subsequent lines.

Based on the analysis delineated in Section 3.1, the reciprocal screws represent forces or torques that may lead to the compliant links' generation of infinitesimal translational, or rotational, motions. These motions can be modelled as the deflection of a linear spring or a rotational spring, respectively, and Fig. 5 displays the stiffness equivalent models of the exoskeleton in Case I and II. Letting τ_a and τ_c denote the reaction forces/torques exerted by the actuators and constraints, respectively, with $\delta q_a = [\delta q_{a1}, \delta q_{a2}]^T$ and $\delta q_c = [\delta q_{c1}, \delta q_{c2}, \delta q_{c3}, \delta q_{c4}]^T$ signifying the corresponding infinitesimal displacement vectors, then the following equations hold

$$\tau_a = k_a \delta q_a, \tau_c = k_c \delta q_c, \tag{19}$$

in which, $k_a = \text{diag}[k_{a1}, k_{a2}]$ and $k_c = \text{diag}[k_{c1}, k_{c2}, k_{c3}, k_{c4}]$. k_{ai} ($i = 1, 2$) and k_{cj} ($j = 1, 2, 3, 4$) represent the stiffness coefficients of the springs related to the actuation forces and constraints, respectively. It should be noted that – in both cases illustrated in Fig. 5 – the k_{c4} spring can be equivalently represented as a combination of different springs [35,37], to match the decomposition of the aforementioned, constrained force. Taking Case I for example, this spring can be regarded as two rotational springs with directions along, and perpendicular to, L_1 , respectively, as illustrated within the red frame of Fig. 5(a). As a result, for Case I, $k_c = \text{diag}[k_{c1}, k_{c2}, k_{c3}, k_{t1}, k_{n1}]$, and in Case II, $k_c = \text{diag}[k_{c1}, k_{c2}, k_{c3}, k_F, k_{t2}, k_{n2}]$. It should be noted that the expression of δq_c will be adjusted accordingly.

For the parallel mechanism, applying the principle of virtual work, while neglecting the gravitational effects, yields

$$w^T \delta D = \tau_a^T \delta q_a + \tau_c^T \delta q_c. \tag{20}$$

In the above expression, $w = [f^T \ m^T]^T$ represents the external wrench that is applied at the reference point of the mobile platform, where f denotes a force vector and m denotes a torque/moment vector. $\delta D = [\delta r^T \ \delta \theta^T]^T$ is the infinitesimal twist of the mobile platform, with δr^T and $\delta \theta^T$ denoting the infinitesimal translational and rotational displacements of the mobile platform, respectively. Substituting (19) into (20) produces

$$w^T \delta D = \delta q_a^T k_a \delta q_a + \delta q_c^T k_c \delta q_c. \tag{21}$$

Considering (13) and (17), δq_a and δq_c can be further expressed as

$$\delta q_a = [J_a \Delta] \delta D, \delta q_c = [J_c \Delta] \delta D. \tag{22}$$

It should be noted that, $T_M = [\omega^T \ v^T]^T$ in (13) and (17), while $\delta D = [\delta r^T \ \delta \theta^T]^T$, therefore in (22), J_a and J_c need to be respectively multiplied with Δ first, to swap their first three columns with their last three columns. Then, (21) can be written as

$$w^T \delta D = \delta D^T [J_a \Delta]^T k_a [J_a \Delta] \delta D + \delta D^T [J_c \Delta]^T k_c [J_c \Delta] \delta D. \tag{23}$$

Table 1
Material parameters of the exoskeleton.

${}^1E={}^2E$	3E	${}^1\nu={}^2\nu$	${}^3\nu$
2.06×10^{11} Pa	1.2×10^{10} Pa	0.304	0.3

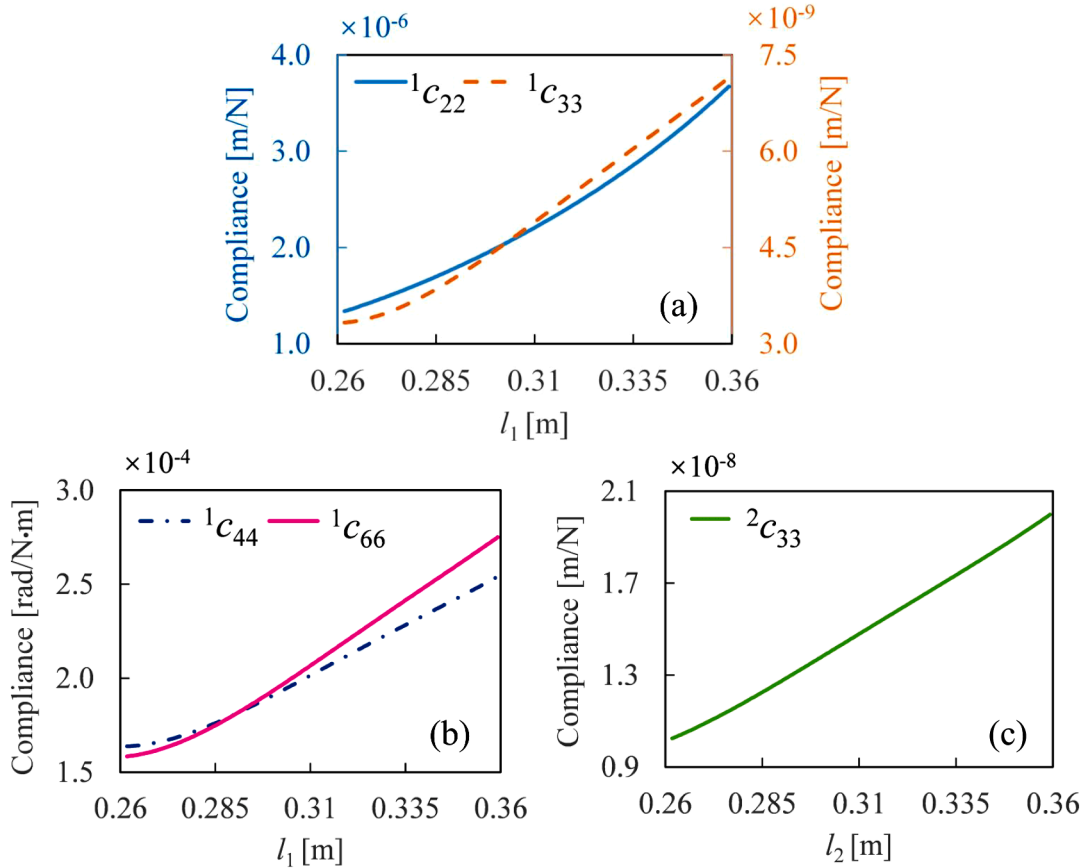


Fig. 7. The relationship between the link length and compliance.

In addition, the relationship between external wrench and infinitesimal twist can be constructed as follows:

$$\mathbf{w} = \mathbf{K}\delta\mathbf{D}, \tag{24}$$

therefore, the overall stiffness matrix \mathbf{K} can be derived as

$$\mathbf{K} = [\mathbf{J}_a\Delta]^T \mathbf{k}_a^T [\mathbf{J}_a\Delta] + [\mathbf{J}_c\Delta]^T \mathbf{k}_c^T [\mathbf{J}_c\Delta] = [\mathbf{J}_a\Delta]^T \mathbf{k}_a [\mathbf{J}_a\Delta] + [\mathbf{J}_c\Delta]^T \mathbf{k}_c [\mathbf{J}_c\Delta]. \tag{25}$$

After rearrangement, (25) turns into

$$\mathbf{K} = [\mathbf{J}\Delta]^T \mathbf{k} [\mathbf{J}\Delta], \tag{26}$$

here, $\mathbf{k} = \begin{bmatrix} \mathbf{k}_a & \mathbf{0} \\ \mathbf{0} & \mathbf{k}_c \end{bmatrix}$ In view of the inverse relationship between the stiffness and compliance matrix, i.e.

$$\mathbf{k}_a = \mathbf{c}_a^{-1}, \mathbf{k}_c = \mathbf{c}_c^{-1}, \tag{27}$$

the elements of \mathbf{k} can be easily derived. To this end, three local frames with axes ${}^k\mathbf{u}$, ${}^k\mathbf{v}$, and ${}^k\mathbf{w}$ ($k = 1, 2, 3$, and hereafter the left superscript is used to differentiate the parameters related to the three links), are built into the three links. As shown in Fig. 6, the local frame of the human shank (i.e. L_3) is coincident with O (x_1, y_1, z_1). For L_1 and L_2 , the ${}^k\mathbf{w}$ -axis ($k = 1, 2$) points along $A_k B_k$, the ${}^k\mathbf{v}$ -axis has the same direction as s_{k2} , and the ${}^k\mathbf{u}$ -axis is determined by the right-hand rule.

Table 2
Geometrical parameters of the exoskeleton.

θ_1	θ_2	h_0	h_1	h_f	$R_1=R_2$	$r_1=r_2$
180°	90°	0.325 m	0 m	0.108m	0.1 m	0.1 m

$$\begin{bmatrix} \delta r_u \\ \delta r_v \\ \delta r_w \\ \delta \theta_u \\ \delta \theta_v \\ \delta \theta_w \end{bmatrix} = \begin{bmatrix} c_{11} & c_{21} & c_{31} & c_{41} & c_{51} & c_{61} \\ c_{12} & c_{22} & c_{32} & c_{42} & c_{52} & c_{62} \\ c_{13} & c_{23} & c_{33} & c_{43} & c_{53} & c_{63} \\ c_{14} & c_{24} & c_{34} & c_{44} & c_{54} & c_{64} \\ c_{15} & c_{25} & c_{35} & c_{45} & c_{55} & c_{65} \\ c_{16} & c_{26} & c_{36} & c_{46} & c_{56} & c_{66} \end{bmatrix} \begin{bmatrix} f_u \\ f_v \\ f_w \\ m_u \\ m_v \\ m_w \end{bmatrix} \tag{28}$$

As the three links are irregular, deformable bodies, their compliances cannot be solved for analytically. Therefore, ANSYS Workbench is employed in this paper to compute the corresponding FEA results. In practice, when only one unit force/torque along/about one axis of the local frame is applied at the reference point, a six-component vector consisting of deformations along and about the three axes can be obtained. According to the definition of compliance described by (28), it can be straightforwardly observed that this vector is exactly one column of the compliance matrix. By changing the direction of the unit force/torque and repeating the above operations, the (6 × 6) compliance matrix can finally be constructed. Further, based on the local frames demonstrated in Fig. 6, the main diagonal elements of the three links' compliance matrices have the greatest influence on the deformations caused by the actuation and constraint forces/torques, and the other elements' effects can be neglected [27]. Therefore, the c_a and c_c elements corresponding to both cases can be finally determined as

$$\begin{aligned} c_{a1} &= {}^1c_{33}, c_{a2} = {}^2c_{33}, \\ c_{c1} &= {}^3c_{11}, c_{c2} = {}^3c_{22}, c_{c3} = {}^3c_{33}, \\ c_{n1} &= c_{n2} = {}^1c_{44}, c_{r1} = c_{r2} = {}^1c_{66}, c_F = {}^1c_{22}. \end{aligned} \tag{29}$$

In this parallel mechanism, the lengths of L_1 and L_2 are variables and the corresponding compliance parameters change in different configurations. Hence, in the simulations, it is necessary to determine the relationship between the link length and compliance. One straightforward means of achieving this is via manual operations, although these are quite complicated and time-consuming. To improve the efficiency, the parameterized method is considered. In computer aided design (CAD) software, SolidWorks, the link lengths of L_1 and L_2 are parameterized as l_1 and l_2 , which can be automatically recognized by ANSYS Workbench as variables (inputs). By changing only these two parameters, the corresponding compliance information (outputs) can be obtained directly. Through several simulation experiments, the relation between the input and output can be built by polynomial fitting.

Table 1 displays the adopted material parameters, in which E represents the Young's modulus and ν is the Poisson ratio. The parameters pertaining to the human shank are extracted from [54]. Inputting these values into Workbench yields ${}^3c_{11}=3.205 \times 10^{-7}$ m/N, ${}^3c_{22}=3.333 \times 10^{-7}$ m/N, ${}^3c_{33}=8.339 \times 10^{-9}$ m/N, as well as the fitting curves shown in Fig. 7. These curves can be well described by the fourth-order polynomials in (30), with correlation coefficient $R^2=1$. Then, the overall stiffness matrix K of any configuration can be obtained via (26) and (27).

$$\begin{aligned} {}^1c_{22} &= 4.9873 \times 10^{-3}l_1^4 - 5.7960 \times 10^{-3}l_1^3 + 2.6232 \times 10^{-3}l_1^2 - 5.2678 \times 10^{-4}l_1 + 4.003 \times 10^{-5}, \\ {}^1c_{33} &= 3.4719 \times 10^{-5}l_1^4 - 4.5842 \times 10^{-5}l_1^3 + 2.2668 \times 10^{-5}l_1^2 - 4.93 \times 10^{-6}l_1 + 3.998 \times 10^{-7}, \\ {}^1c_{44} &= 1.0499l_1^4 - 1.3726l_1^3 + 0.6716 \times 10^{-7}l_1^2 - 0.1447 \times 10^{-4}l_1 + 0.0117, \\ {}^1c_{66} &= 0.9708 \times 10^{-1}l_1^4 - 1.2854l_1^3 + 0.6374l_1^2 - 0.1389l_1 + 0.0113, \\ {}^2c_{33} &= 5.5302 \times 10^{-5}l_2^4 - 6.9898 \times 10^{-5}l_2^3 + 3.3103 \times 10^{-5}l_2^2 - 6.8594 \times 10^{-6}l_2 + 5.3163 \times 10^{-7}. \end{aligned} \tag{30}$$

4. Stiffness evaluation

4.1. Workspace of the exoskeleton

As discussed in [22], the rotational properties of the novel exoskeleton are summarized as two different cases depending on the relative positions of points O and P. This paper focuses exclusively on the stiffness analysis of the second case in [22], given its superior performance in terms of satisfying the rehabilitation requirements. The specific geometrical parameters of the corresponding configuration – which are designed based on the anthropometric data provided in [55] – are listed in Table 2. Under this arrangement, the rotation matrix of the 2-DOF exoskeleton can be constructed as follows

$$R = R_{y_1}(\beta)R_{x_1}(\alpha) = \begin{bmatrix} c\beta & 0 & s\beta \\ 0 & 1 & 0 \\ -s\beta & 0 & c\beta \end{bmatrix} \begin{bmatrix} 1 & 0 & 0 \\ 0 & c\alpha & -s\alpha \\ 0 & s\alpha & c\alpha \end{bmatrix} = \begin{bmatrix} c\beta & sas\beta & cas\beta \\ 0 & c\alpha & -s\alpha \\ -s\beta & sac\beta & cac\beta \end{bmatrix}, \tag{31}$$

in which, α and β are Euler angles about the x_1 -axis and y_1 -axis (as indicated in Fig. 2), which also respectively represent the I/E and D/P motion angles. Meanwhile, it is known from the analysis conducted in [22] that, when $\beta = 0$, the exoskeleton has a Case I configuration; otherwise, the exoskeleton is in a Case II configuration. The purpose of conducting a workspace analysis for this

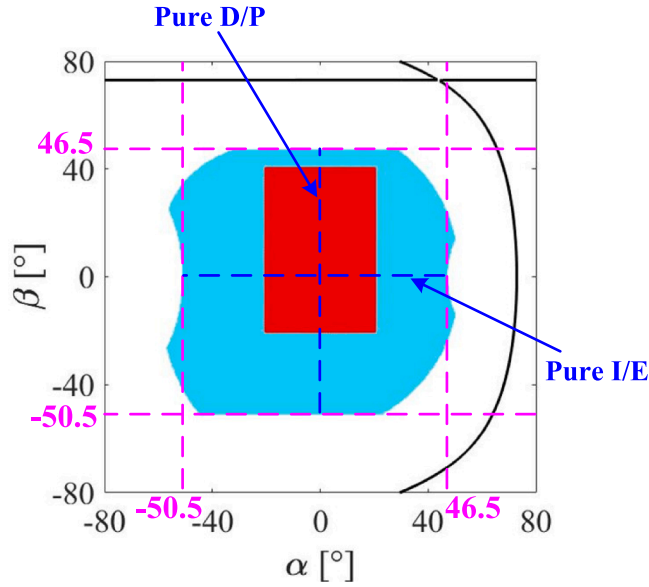


Fig. 8. Workspace of the exoskeleton.

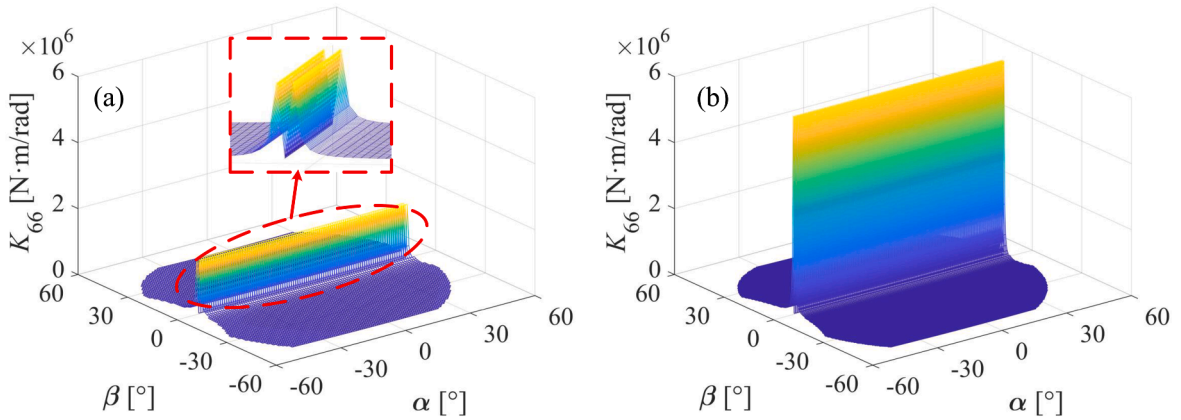


Fig. 9. Angular stiffness about w-axis computed with (a) coarse meshes and (b) refined meshes.

exoskeleton is to determine all the possible α - β combinations, under certain geometrical constraints.

Specifically, the closed-loop equations of L_1 and L_2 need to be built initially, using (31). Based on these, l_1 and l_2 can be subsequently derived as (32) – one may refer to [22] for the detailed deduction processes.

$$\begin{aligned} l_1 &= \sqrt{(R_1 - r_1 c\beta)^2 + (r_1 s\beta - h_0)^2}, \\ l_2 &= \sqrt{-2r_2 s\alpha c\beta h_0 - 2R_2 r_2 c\alpha + R_2^2 + r_2^2 + h_0^2}. \end{aligned} \tag{32}$$

Then, by considering the actuators' stroke lengths (0.15 m) and joint work range constraints (60° for the U-joint, 10° for the S-joint), the workspace can be calculated in Matlab. As illustrated in Fig. 8, the irregular light blue area is the computed, theoretical workspace, which completely covers the prescribed rehabilitation ROM depicted by the red rectangle. By denoting the rotational angles about the positive axis directions as positive, and the angles about the opposite directions as negative, then the prescribed ROM is $[-20^\circ, 20^\circ]$ for I/E motions, and $[-20^\circ, 40^\circ]$ for D/P motions [12,56]. For the current settings, the achievable range is $[-50.5^\circ, 46.5^\circ]$ when performing only I/E and D/P motions. Meanwhile, the reachable region of the exoskeleton is singularity-free, and is located far away from the singularity loci indicated by the black curves in Fig. 8.

4.2. Modified SBM and numerical verification

By incorporating geometrical parameters, the (6×6) stiffness matrix \mathbf{K} of reference point F can be derived within the workspace –

using the method introduced in Section 3.2 – with elements K_{ij} (i, j are column and row numers, respectively). The translational (rotational) stiffness along (about) each axis of the F frame can be defined by the main diagonal elements of \mathbf{K} — $K_{11} \sim K_{66}$. However, this primitive SBM does not produce reasonable results. Fig. 9 displays the numerical results relating to the angular stiffness about the w -axis (K_{66}). As indicated in the inset of (a), the stiffness values increase abruptly when β approaches zero, and this corresponds to the transformation from Case II to Case I. Hereafter, for convenience of expression, the configuration corresponding to the critical state of transition between the two cases is defined as the transition configuration. It can be found that, the results pertaining to these configurations and their adjacent configurations are physically unrealisable, and greatly depend on the mesh sizes. When the meshes are refined, the positions of the protrusions move much closer to zero on the β -axis, and the protrusions' heights also exhibit an obvious rise (as shown in Fig. 9(b)). This implies that K_{66} (of the discussed configurations) will approach infinity using sufficiently high mesh granularity, which further reveals that the rotational deformations about the w -axis will disappear at these configurations. Given the fact that the links are assumed to be deformable bodies, and that there are no singular positions in the workspace, the simulated scenario predicted by the computational results (based on the conventional SBM) is not practically realisable. Further, the following lines give the reasons for this phenomenon.

Since the transition configurations belong to Case II, the overall Jacobian matrix is constructed as $\mathbf{J}_{II} = (\mathbf{J}_a \mathbf{J}_{c2})^T$. Substituting it into (26) yields

$$\mathbf{K}_{II} = \begin{bmatrix} \mathbf{K}_{II-1} & \mathbf{K}_{II-2} \\ \mathbf{K}_{II-3} & \mathbf{K}_{II-4} \end{bmatrix}_{6 \times 6}, \tag{33}$$

in which, $\mathbf{K}_{II-1} \sim \mathbf{K}_{II-4}$ are (3×3) matrices, which can be expressed as

$$\begin{aligned} \mathbf{K}_{II-1} &= \sum_{i=1}^2 k_{ai} \mathbf{s}_{i3} \mathbf{s}_{i3}^T + \sum_{j=1}^3 k_{cj} \mathbf{s}_{3j} \mathbf{s}_{3j}^T + k_F \mathbf{s}_{12} \mathbf{s}_{12}^T, \\ \mathbf{K}_{II-2} &= \sum_{i=1}^2 k_{ai} \mathbf{s}_{i3} (\mathbf{b}_i \times \mathbf{s}_{i3})^T + \sum_{j=1}^3 k_{cj} \mathbf{s}_{3j} (\mathbf{h} \times \mathbf{s}_{3j})^T + k_F \mathbf{s}_{12} (\mathbf{b}_1 \times \mathbf{s}_{12})^T, \\ \mathbf{K}_{II-3} &= \sum_{i=1}^2 k_{ai} (\mathbf{b}_i \times \mathbf{s}_{i3}) \mathbf{s}_{i3}^T + \sum_{j=1}^3 k_{cj} (\mathbf{h} \times \mathbf{s}_{3j}) \mathbf{s}_{3j}^T + k_F (\mathbf{b}_1 \times \mathbf{s}_{12}) \mathbf{s}_{12}^T, \\ \mathbf{K}_{II-4} &= \sum_{i=1}^2 k_{ai} (\mathbf{b}_i \times \mathbf{s}_{i3}) (\mathbf{b}_i \times \mathbf{s}_{i3})^T + \sum_{j=1}^3 k_{cj} (\mathbf{h} \times \mathbf{s}_{3j}) (\mathbf{h} \times \mathbf{s}_{3j})^T \\ &\quad + k_F (\mathbf{b}_1 \times \mathbf{s}_{12}) (\mathbf{b}_1 \times \mathbf{s}_{12})^T + k_{r2} p_{r2}^2 \mathbf{s}_{13} \mathbf{s}_{13}^T + k_{n2} p_{n2}^2 (\mathbf{s}_{12} \times \mathbf{s}_{13}) (\mathbf{s}_{12} \times \mathbf{s}_{13})^T. \end{aligned} \tag{34}$$

In the configurations for which physically unrealisable results are obtained, \mathbf{s}_{11} and \mathbf{s}_{15} are almost parallel, but have an intersection point near infinity. Meanwhile, according to [22], the exoskeleton constructed based on geometrical parameters listed in Table 2 has a decoupled control feature. To be more specific, the rotation angles α and β are independently dictated by L_2 and L_1 links, respectively. Therefore, when β approaches zero (regardless of the α angle's value), L_1 gets infinitely close to its initial status, i.e. vertical to the brace, where, $\mathbf{s}_{13} \perp \mathbf{s}_{11}$ and $\mathbf{s}_{13} \perp \mathbf{s}_{12}$. Accordingly, \mathbf{s}_{13} has an approximate expression of $[0 \ 0 \ -1]^T$, and the $(\mathbf{s}_{12} \times \mathbf{s}_{13})$ counterpart is $[-1 \ 0 \ 0]^T$. Then, \mathbf{K}_{II-4} can be approximately expressed as follows

$$\mathbf{K}_{II-4} = \mathbf{k}_{sum} + \begin{pmatrix} 0 & 0 & 0 \\ 0 & 0 & 0 \\ 0 & 0 & k_{r2} p_{r2}^2 \end{pmatrix} + \begin{pmatrix} k_{n2} p_{n2}^2 & 0 & 0 \\ 0 & 0 & 0 \\ 0 & 0 & 0 \end{pmatrix} = \mathbf{k}_{sum} + \begin{pmatrix} k_{n2} p_{n2}^2 & 0 & 0 \\ 0 & 0 & 0 \\ 0 & 0 & k_{r2} p_{r2}^2 \end{pmatrix}. \tag{35}$$

in which, \mathbf{k}_{sum} represents the sum of the first three terms in the \mathbf{K}_{II-4} expression displayed via (34). Based on the definitions of p_{l2} and p_{n2} given in Section 3.1, it is straightforward to find that when \mathbf{s}_{12} and \mathbf{s}_{15} intersect at infinity, p_{l2} has an infinite value, while p_{n2} 's magnitude can be neglected. Meanwhile, the elements in the matrix \mathbf{k}_{sum} have finite magnitudes, and when the exoskeleton configurations change from Case II to Case I, they also change continuously. Based on the above, only the last main diagonal element of \mathbf{K}_{II-4} , increases abruptly when the transition happens. Since K_{44} , K_{55} and K_{66} are respectively the first, second and third main diagonal elements of \mathbf{K}_{II-4} , then K_{66} will behave in a way similar to that shown in Fig. 9; K_{44} and K_{55} vary smoothly. As for $K_{11} \sim K_{33}$, they can be extracted from \mathbf{K}_{II-1} , and due to similar reasons as those for K_{44} and K_{55} , there will not appear any abrupt protrusions in the variations of the three elements.

Before proceeding to the stiffness discussion of the exoskeleton, the SBM needs to be modified first to address the unreasonable protrusion problem. An observation of the units of the overall Jacobian matrix reveals that the first three columns' elements are expressed in units of length, while the last three columns' elements are dimensionless. Similar circumstances also appear in the published work/s that employ the SBM. The authors of [24,34,35] defined a characteristic length of fixed value to be divided by the non-dimensionless items in the Jacobian matrix, for the purpose of unit homogenization. In [37–39], this characteristic length is selected as unit one, as is also the case in Section 3.1. In all these examples, the magnitude order of the modulus of the non-dimensionless items in the Jacobian is not significantly different. Meanwhile, based on the analysis above and the expression of \mathbf{J}_{c2} , the situation discussed in this paper is different, and the conventional method can therefore not be directly applied. Therefore, a specific strategy is proposed for the purpose of homogenizing the Jacobian. Specifically, \mathbf{J}_{c2} is recast into (36)

Table 3
Results comparisons.

Example	Method	δr_w (m)	$\delta \theta_u$ (rad)	$\delta \theta_v$ (rad)	$\delta \theta_w$ (rad)
1 ($\alpha=0^\circ, \beta=0^\circ$)	FEA	8.3360×10^{-9}	2.4187×10^{-6}	1.3622×10^{-6}	1.9986×10^{-4}
	Modified SBM	8.3387×10^{-9}	2.4662×10^{-6}	1.3923×10^{-6}	2.1775×10^{-4}
2 ($\alpha=0^\circ, \beta=1^\circ$)	FEA	8.0318×10^{-9}	2.4190×10^{-6}	1.3551×10^{-6}	1.9539×10^{-4}
	Modified SBM	8.2312×10^{-9}	2.4675×10^{-6}	1.4057×10^{-6}	2.1512×10^{-4}
3 ($\alpha=0^\circ, \beta=40^\circ$)	FEA	5.4324×10^{-9}	2.4187×10^{-6}	2.6396×10^{-6}	1.2302×10^{-4}
	Modified SBM	5.7051×10^{-9}	2.3396×10^{-6}	2.8156×10^{-6}	1.4050×10^{-4}

$$J_{ch2} = \begin{pmatrix} (\mathbf{h} \times \mathbf{s}_{31})^T & \mathbf{s}_{31}^T \\ (\mathbf{h} \times \mathbf{s}_{32})^T & \mathbf{s}_{32}^T \\ (\mathbf{h} \times \mathbf{s}_{33})^T & \mathbf{s}_{33}^T \\ d^{-1}(\mathbf{b}_1 \times \mathbf{s}_{12})^T & \mathbf{s}_{12}^T \\ p_{12}d^{-1}\mathbf{s}_{13}^T & \mathbf{0}^T \\ p_{n2}d^{-1}(\mathbf{s}_{12} \times \mathbf{s}_{13})^T & \mathbf{0}^T \end{pmatrix}_{6 \times 6}, \tag{36}$$

in which, $d=|\mathbf{r}_C-\mathbf{b}_1|$, is defined as a dynamic characteristic length that changes with the positions of Point C. It is used to homogenize the items derived from cS of Case II. The other non-dimensionless items in J_{c2} , and those of J_a , are homogenized by unit one.

This modified Jacobian matrix ensures a smooth transition of K_{66} from Case II to Case I, while providing an acceptable estimate of the proposed design’s stiffness. The variations of K_{66} , computed by the modified SBM, are displayed in Fig. 11(d), and the method verifications results are presented in Table 3. In this table, three representative instances are selected. Example 1 is actually the initial configuration of the mechanism (belonging to Case I, in which \mathbf{s}_{11} and \mathbf{s}_{15} are completely parallel), and Example 2 is selected to represent the situation where \mathbf{s}_{11} and \mathbf{s}_{15} are almost parallel. Comparatively, Example 3 indicates the case where the footplate moves to the right bound of the prescribed ROM of D/P motions, and under this circumstance, \mathbf{s}_{11} and \mathbf{s}_{15} are far away from the parallel state (Fig. 10(c)). From the FEA results of Example 1 and 2, one can observe that, when \mathbf{s}_{11} and \mathbf{s}_{15} change from the completely parallel state to the almost-parallel state, the stiffness indices do not exhibit significant variation. This further proves the incorrectness of the results shown in Fig. 9. Meanwhile, in all the three representative examples, the results produced by the modified SBM accurately match those generated by the FEA. Fig. 10 illustrates the linear deformations of the entire mechanism when a unit force is applied to the reference point F, along the w -axis – this serves as a demonstration of the FEA simulations.

4.3. Stiffness assessment of the exoskeleton

In the dynamical gait rehabilitation processes, the external disturbances applied onto the footplate can be deemed equivalent to the combination of the vertical force and the three directional torques. Therefore, the exoskeleton’s capacity to resist against these wrenches is of utmost concern, and this can be indicated by the stiffness factors [33] K_{33} , K_{44} , K_{55} and K_{66} . Fig. 11 presents the distributions of these stiffness coefficients throughout the workspace.

Since the exoskeleton has an asymmetric architecture, coefficients K_{33} , K_{44} , and K_{55} are distributed asymmetrically. However, as an exception, K_{66} has an approximately axisymmetric distribution feature about the w -axis, which is attributed to the fact that the rotation about the vertical axis is totally confined as a result of the mechanism’s constraint links. As seen from Fig. 11(a), the change of β has a significant impact on K_{33} . When β changes from negative to positive values (i.e. from the dorsiflexion to plantarflexion motion), K_{33} displays a prominent increase – this is a desirable feature for dynamical rehabilitation. During a gait cycle, transitioning from dorsiflexion to plantarflexion corresponds to the push-off phase, which requires a larger propulsive force to move the human body forward. Therefore, K_{33} is expected to increase during this phase. As a comparison, α has a smaller influence on K_{33} , while K_{44} ’s variation trend is more obvious along the α -axis. As indicated in Fig. 11(b), K_{44} decreases first and increases subsequently, with its minimum value occurring on the $\alpha > 0^\circ$ side, when the ankle-foot complex is in the inversion configuration. K_{55} is sensitive to both the rotation angles, and also has the most complex transitional pattern amongst the four main diagonal elements. Its maximum and minimum values correspond to the points in the workspace’s bottom right, and top left, corners, respectively. Meanwhile, it can be concluded that the minimum values of K_{44} and K_{55} are larger than the maximum value of K_{66} .

As evinced by the clinical evidence reported in [57], assistance of I/E and D/P promotes a comprehensive gait rehabilitation of patients. Hence, the variations of the four stiffness parameters – when performing only I/E or D/P motions – can be further extracted. As shown in Fig. 12, these parameters’ evolutions conform to the features described above. Particularly, for D/P motions, K_{44} (angular stiffness about the u -axis) is almost unchanged. A similar conclusion can be drawn for K_{55} (angular stiffness about the v -axis), when performing only I/E motions.

Additionally, it is shown that the stiffness of a parallel mechanism is bounded by the minimum and maximum eigenvalues of the overall stiffness matrix [58], which are depicted as the minimum stiffness (K_{min}) and maximum stiffness (K_{max}), respectively. The evaluation of these two performance indices can provide a global view of the exoskeleton’s stiffness. Also, to ensure accuracy, the mechanism’s minimum stiffness should be larger than a specified value. On the basis of the above, apart from the aforementioned

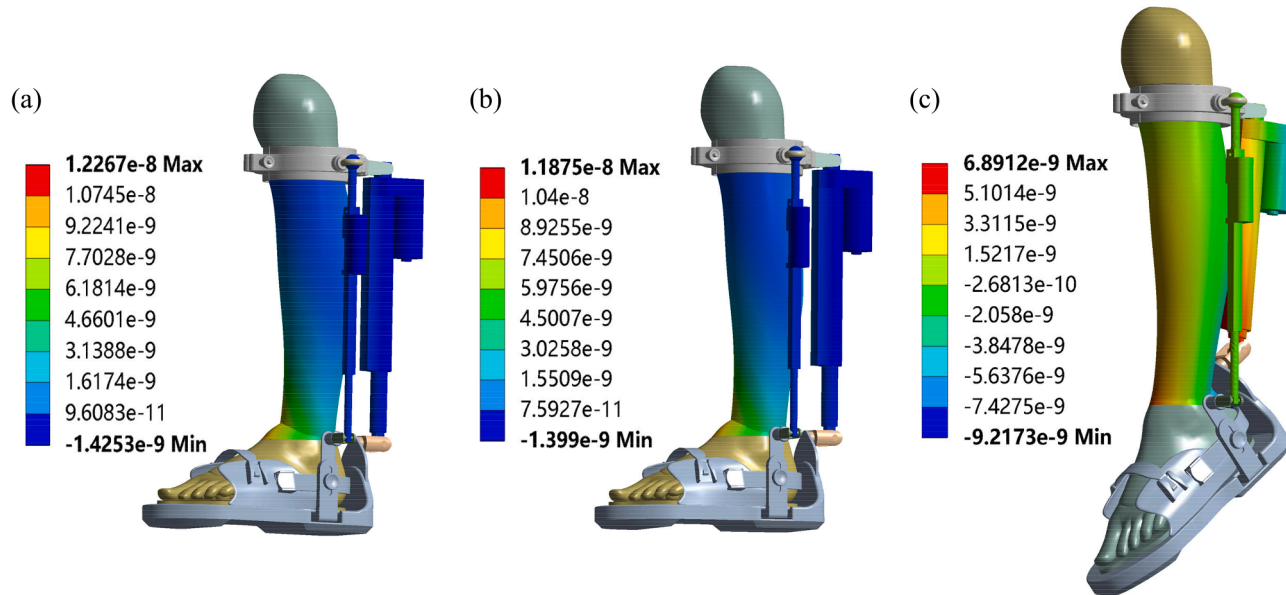


Fig. 10. Linear deformations along w-axis in (a) Example 1, (b) Example 2, and (c) Example 3.

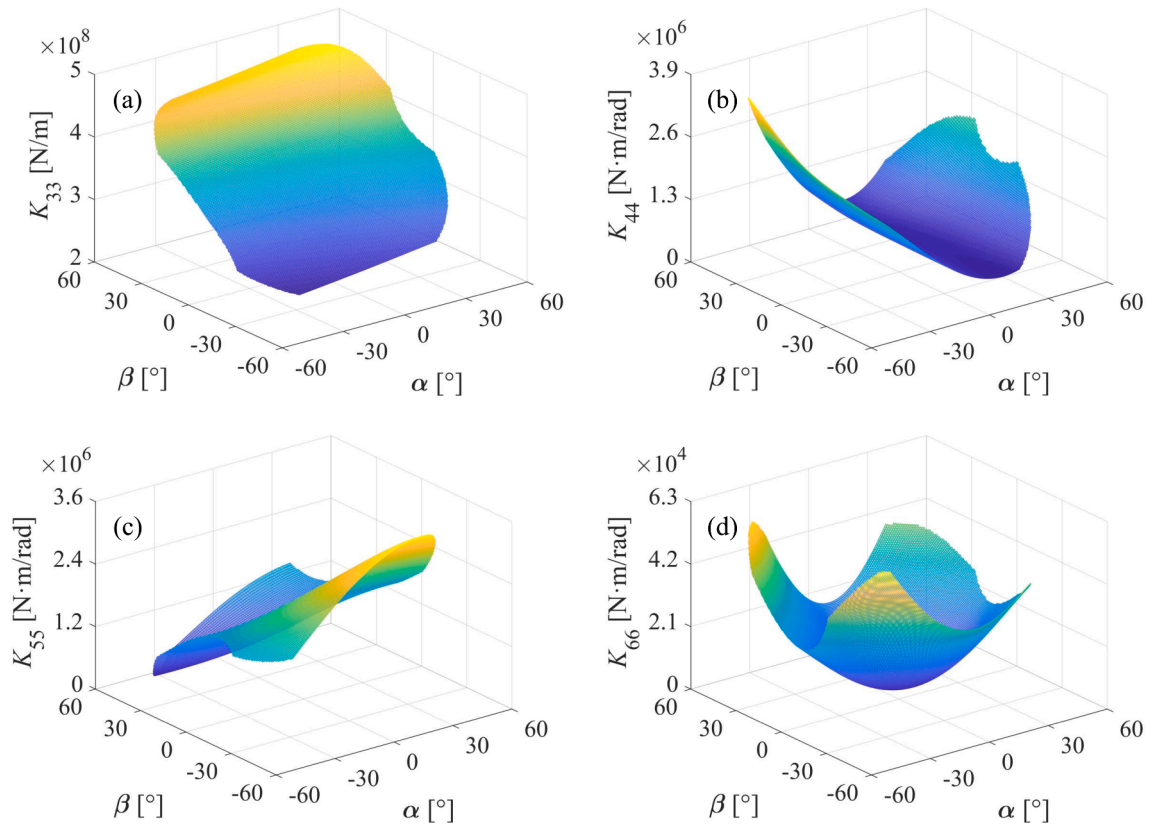


Fig. 11. Stiffness distributions over workspace: (a) linear stiffness along w -axis, (b) angular stiffness about u -axis, (c) angular stiffness about v -axis, and (d) angular stiffness about w -axis.

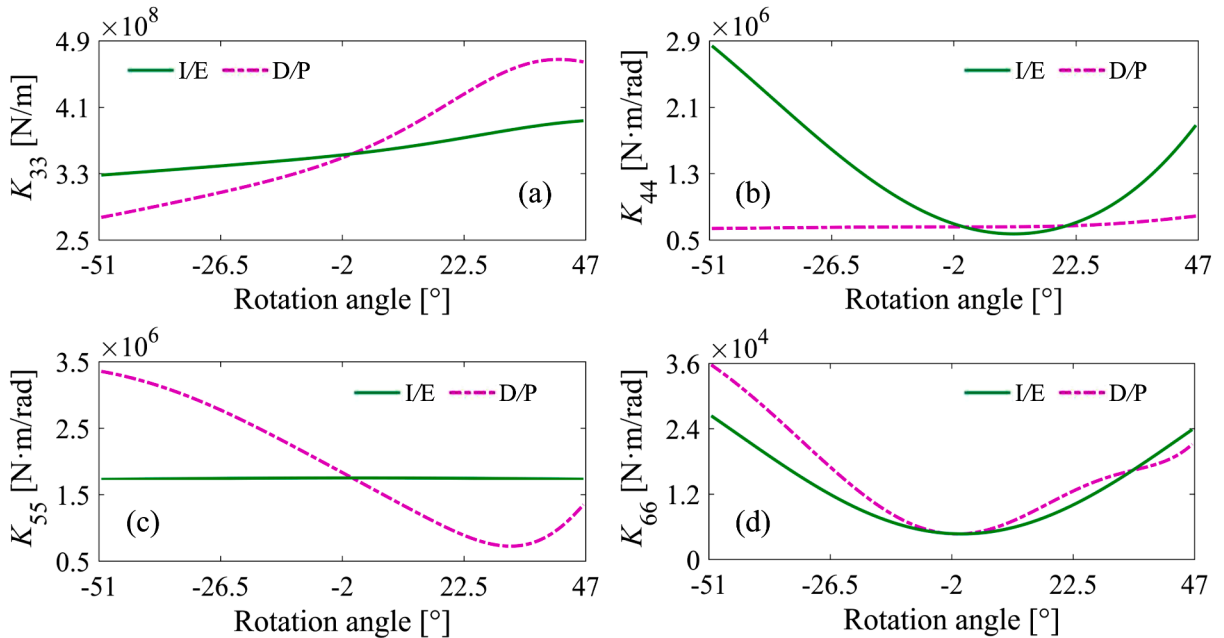


Fig. 12. Variations of K_{33} - K_{66} when the exoskeleton performs only I/E or D/P motions.

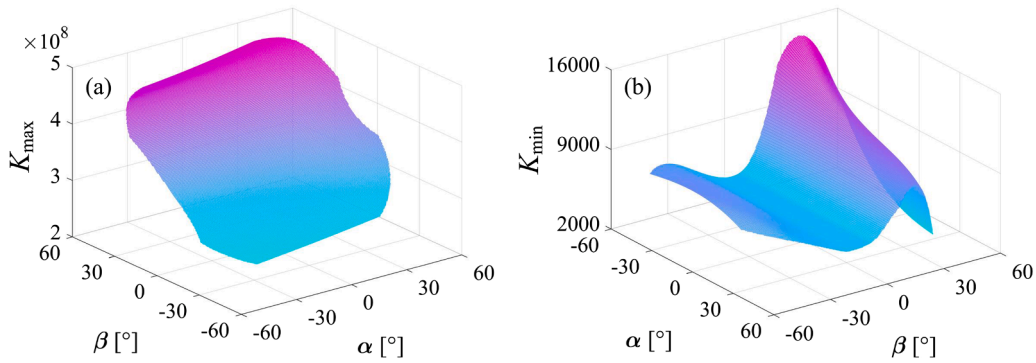


Fig. 13. Distributions of K_{\max} and K_{\min} throughout the workspace.

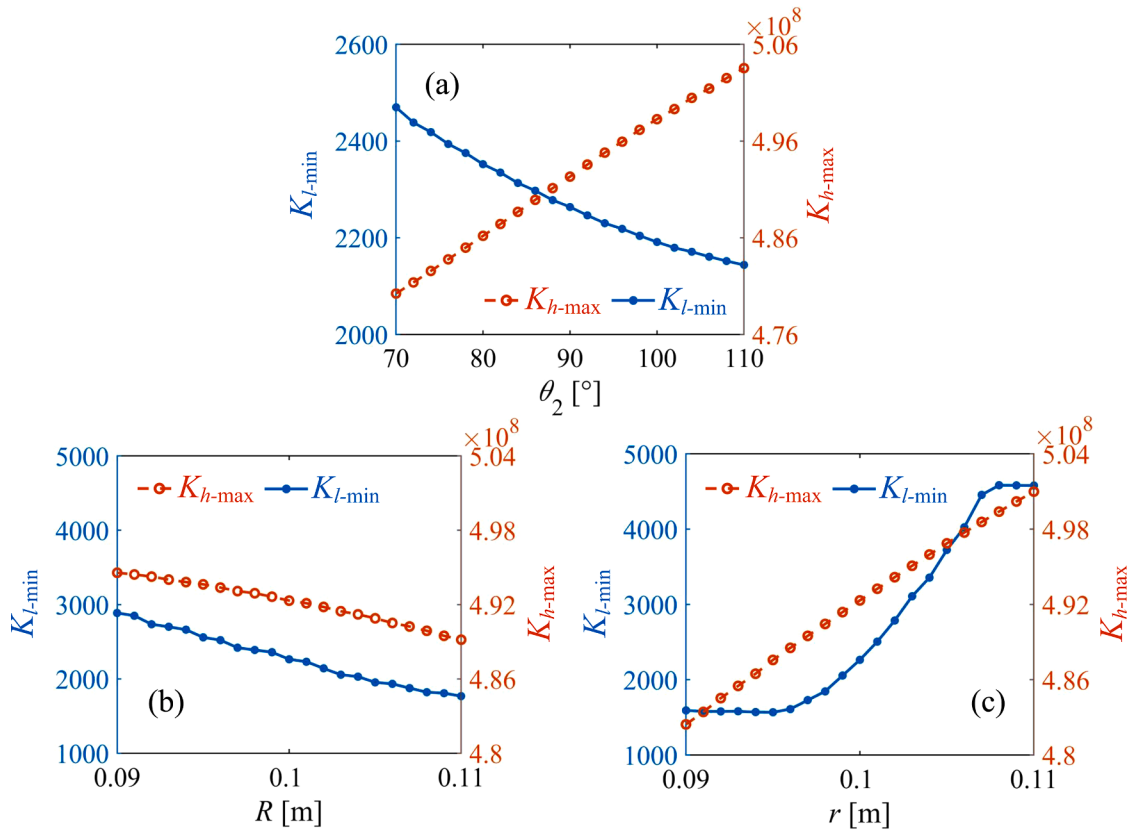


Fig. 14. Performance indices of $K_{l-\min}$ and $K_{h-\max}$ versus design parameters.

stiffness factors, K_{\min} and K_{\max} are selected as additional stiffness indices for evaluation of the exoskeleton’s stiffness performance.

Fig. 13 displays the corresponding calculation results, from which it is clear that the variational tendency of K_{\max} is similar to that of K_{33} , and in the prescribed rehabilitation workspace, the highest value of K_{\max} (i.e. $K_{h-\max}$) is 4.8152×10^8 . The extrema of K_{\min} are on the $\beta > 0^\circ$ side, and under the current arrangement, the smaller extremum (i.e. $K_{l-\min}$) is 2325.6, which located outside of the prescribed ROM (with the coordinate of $\alpha=29^\circ, \beta=46.5^\circ$). Meanwhile, $K_{l-\min}$, in the prescribed ROM, occurs around the initial position ($\alpha=0^\circ, \beta=0^\circ$), with a magnitude of 4608.1 (nearly twice as large as 2325.6). In the following analysis, the change of $K_{l-\min}$ and $K_{h-\max}$, along with the variations of the architectural parameters, are further explored. Without loss of generality, the discussion pertains to the complete workspace of the design.

Fig. 14 demonstrates the obtained results, in which $R = R_1=R_2$ and $r = r_1=r_2$. (a) indicates that $K_{l-\min}$ and $K_{h-\max}$ display converse variational tendencies, w.r.t each other, as θ_2 increases; $K_{h-\max}$ increases in an approximately linear manner, and $K_{l-\min}$ decreases monotonically. From Fig. 14(b), one can observe that the trends for the two indices are the same. Similar conclusions can be drawn from Fig. 14(c) in the range of [0.096 m, 0.108 m]. Outside this range, $K_{l-\min}$ is almost unchanged, although $K_{h-\max}$ continues to

increase. As an overall trend, the increase of R has the same effect as the decrease of r . However, when R and r vary within the aforementioned range, $K_{l\text{-min}}$ and $K_{h\text{-max}}$ in Fig. 14(c) have larger spans. In summary, the most effective way to improve the value of $K_{l\text{-min}}$ is to enlarge r in the range of [0.096 m, 0.108 m].

5. Conclusions

This paper presents a stiffness analysis of a novel ankle rehabilitation exoskeleton in a parallel architecture. The employed U-P-U link provides a torque when the mechanism performs only I/E motions, and a force during all other motions. Before performing the stiffness modelling, two configuration cases are classified. Further analysis reveals that primitive SBM fails to provide reliable results for the angular stiffness of interest, K_{66} , in transition configurations and their adjacent configurations. As a result, a modified SBM is proposed. The comparison with the FEA results demonstrates the effectiveness of the proposed strategy within the workspace.

Considering the application scenario of the exoskeleton, the distribution of the linear stiffness along the w -axis (K_{33}), and that of the three angular stiffnesses (K_{44} – K_{66}), are presented. From these results, it can be observed that K_{33} displays a desired variational tendency for dynamical rehabilitation exercises. K_{66} has the smallest values amongst the three angular parameters, albeit exhibiting an approximately axisymmetric distribution about the w -axis. The results also show that, in individual D/P motions, K_{44} is almost unchanged; a similar conclusion can be drawn about K_{55} when the exoskeleton performs only I/E motions.

The minimum stiffness, K_{min} , and maximum stiffness, K_{max} , are also adopted to give a global picture of the mechanism's stiffness. These values demonstrate that K_{max} has a similar variational trend as K_{33} , and the minimum value of K_{min} is located near the initial position in the prescribed ROM. Meanwhile, after an investigation of the effects of the architectural parameters (θ_2 , R , r) on $K_{l\text{-min}}$ and $K_{h\text{-max}}$, it is found that enlarging r in the range of [0.096 m, 0.108 m] is the most effective way to improve the exoskeleton's stiffness performance, under the condition that the other architectural parameters remain fixed.

Declaration of Competing Interest

The authors declare that they have no known competing financial interests or personal relationships that could have appeared to influence the work reported in this paper.

Acknowledgement

The authors gratefully acknowledge the support from the Engineering and Physical Sciences Research Council (EPSRC) of the United Kingdom under Grant No. EP/S019790/1, the Science, Technology and Innovation Commission of Shenzhen Municipality under Grant ZDSYS20200811143601004, and China Scholarship Council (CSC).

References

- [1] I. Díaz, J.J. Gil, E. Sánchez, Lower-limb robotic rehabilitation: literature review and challenges, *J. Robot.* 2011 (2) (2011) 1–11.
- [2] C. Wang, Y. Fang, S. Guo, C. Zhou, Design and kinematic analysis of redundantly actuated parallel mechanisms for ankle rehabilitation, *Robotica* 33 (2) (2015) 366–384.
- [3] W. Huo, S. Mohammed, J.C. Moreno, Y. Amirat, Lower limb wearable robots for assistance and rehabilitation: a state of the art, *IEEE Syst. J.* 10 (3) (2016) 1068–1081.
- [4] M. Dong, Y. Zhou, J. Li, X. Rong, W. Fan, X. Zhou, Y. Kong, State of the art in parallel ankle rehabilitation robot: a systematic review, *J. Neuroeng. Rehabil.* 18 (1) (2021) 1–15.
- [5] P.K. Jamwal, S. Hussain, S.Q. Xie, Review on design and control aspects of ankle rehabilitation robots, *Disabil. Rehabil. Assist. Technol.* 10 (2) (2015) 93–101.
- [6] M.J. Girone, G.C. Burdea, M. Bouzit, 'Rutgers ankle' orthopedic rehabilitation interface, *Am. Soc. Mech. Eng. Dyn. Syst. Control Div. DSC* 67 (1999) 305–312.
- [7] J.S. Dai, C.P. Massicks, An equilateral ankle rehabilitation device based on parallel mechanisms, *BMC Psychiatry* 12 (1) (1999) 229.
- [8] J.S. Dai, T. Zhao, C. Nester, Sprained ankle physiotherapy based mechanism synthesis and stiffness analysis of a robotic rehabilitation device, *Auton. Robot* 16 (2) (2004) 207–218.
- [9] G. Liu, J. Gao, H. Yue, X. Zhang, G. Lu, Design and kinematics analysis of parallel robots for ankle rehabilitation, *IEEE Int. Conf. Intell. Robot. Syst.* (2006) 253–258.
- [10] J.A. Saglia, J.S. Dai, D.G. Caldwell, Geometry and kinematic analysis of a redundantly actuated parallel mechanism that eliminates singularities and improves dexterity, *J. Mech. Des.* 130 (12) (2008), 124501.
- [11] J.A. Saglia, N.G. Tsagararakis, J.S. Dai, D.G. Caldwell, A high-performance redundantly actuated parallel mechanism for ankle rehabilitation, *Int. J. Rob. Res.* 28 (9) (2009) 1216–1227.
- [12] A. Erdogan, B. Celebi, A.C. Satici, V. Patoglu, Assist on-ankle: a reconfigurable ankle exoskeleton with series-elastic actuation, *Auton. Robots* 41 (3) (2017) 743–758.
- [13] Y.H. Tsoi, S.Q. Xie, A.E. Graham, Design, modeling and control of an ankle rehabilitation robot, *Stud. Comput. Intell.* 177 (2009) 377–399.
- [14] M. Malosio, S.P. Negri, N. Pedrocchi, F. Vicentini, M. Caimmi, L. Molinari Tosatti, A spherical parallel three degrees-of-freedom robot for ankle-foot neuro-rehabilitation, *Proc. Annu. Int. Conf. IEEE Eng. Med. Biol. Soc. EMBS* (2012) 3356–3359.
- [15] C. Wang, Y. Fang, S. Guo, Y. Chen, Design and kinematical performance analysis of a 3-RUS/RRR redundantly actuated parallel mechanism for ankle rehabilitation, *J. Mech. Robot.* 5 (4) (2013) 1–11.
- [16] Y. Du, R. Li, D. Li, S. Bai, An ankle rehabilitation robot based on 3-RRS spherical parallel mechanism, *Adv. Mech. Eng.* 9 (8) (2017) 1–8.
- [17] T.C. Chang, X.D. Zhang, Kinematics and reliable analysis of decoupled parallel mechanism for ankle rehabilitation, *Microelectron. Reliab.* 99 (March) (2019) 203–212.
- [18] C.-H. Kuo, J.S. Dai, Kinematics of a fully-decoupled remote center-of-motion parallel manipulator for minimally invasive surgery, *J. Med. Dev.* 6 (2) (2012), 021008.
- [19] H.I. Krebs, N. Hogan, Therapeutic Robotics: a Technology Push, *Proc. IEEE* 94 (9) (2006) 1727–1737.
- [20] H. Wang, W. Li, H. Liu, J. Zhang, S. Liu, Conceptual design and dimensional synthesis of a novel parallel mechanism for lower-limb rehabilitation, *Robotica* 37 (3) (2019) 469–480.

- [21] K. Bharadwaj, T.G. Sugar, J.B. Koeneman, E.J. Koeneman, Design of a robotic gait trainer using spring over muscle actuators for ankle stroke rehabilitation, *J. Biomech. Eng.* 127 (6) (2005) 1009–1013.
- [22] T. Wang, E. Olivoni, E. Spyraeos-Papastavridis, R.J. O'Connor, J.S. Dai, Novel design of a rotation centre auto-matched ankle rehabilitation exoskeleton with decoupled control capacity, *ASME. J. Mech. Des.* 144 (5) (2021), 053301.
- [23] T. Wang, E. Spyraeos-Papastavridis, J.S. Dai, Design and analysis of a novel reconfigurable ankle rehabilitation exoskeleton capable of matching the mobile biological joint centre in real-time, *J. Mech. Robot.* 15 (February) (2022) 1–19.
- [24] H.B. Tian, H.W. Ma, J. Xia, K. Ma, Z.Z. Li, Stiffness analysis of a metamorphic parallel mechanism with three configurations, *Mech. Mach. Theory* 142 (2019), 103595.
- [25] M. Lee, et al., A compact ankle exoskeleton with a multi-axis parallel linkage mechanism, *IEEE/ASME Trans. Mechatronics*. 26 (1) (2021) 191–202.
- [26] C.Z. Wang, Y.F. Fang, S. Guo, C.C. Zhou, Design and kinematic analysis of redundantly actuated parallel mechanisms for ankle rehabilitation, *Robotica* 33 (2) (2015) 366–384.
- [27] C. Zhao, Z. Chen, J. Song, X. Wang, H. Ding, Deformation analysis of a Novel 3-DOF parallel spindle head in gravitational field, *Mech. Mach. Theory* 154 (2020), 104036.
- [28] A. Pashkevich, D. Chablat, P. Wenger, Stiffness analysis of overconstrained parallel manipulators, *Mech. Mach. Theory* 44 (5) (2009) 966–982.
- [29] T. Sun, B. Lian, Y. Song, Stiffness analysis of a 2-DOF over-constrained RPM with an articulated traveling platform, *Mech. Mach. Theory* 96 (2016) 165–178.
- [30] C.M. Gosselin, Stiffness mapping for parallel manipulators, *IEEE Trans. Robot. Autom.* 6 (3) (1990) 377–382.
- [31] C.M. Gosselin, D. Zhang, Stiffness analysis of parallel mechanisms using a lumped model, *Int. J. Robot. Autom.* 17 (1) (2002) 17–27.
- [32] T. Sun, S.F. Yang, B.B. Lian, *Finite and Instantaneous Screw Theory in Robotic Mechanism*, Springer, Singapore, 2020.
- [33] Joshi, S.A., and Tsai, L., 2002, "Jacobian analysis of limited-DOF parallel manipulators," *DETC2002/MECH-34238*, Montreal, Canada, pp. 254–258.
- [34] Y. Li, Q. Xu, Stiffness analysis for a 3-PUU parallel kinematic machine, *Mech. Mach. Theory* 43 (2) (2008) 186–200.
- [35] Q. Xu, Y. Li, An investigation on mobility and stiffness of a 3-DOF translational parallel manipulator via screw theory, *Robot. Comput. Integr. Manuf.* 24 (3) (2008) 402–414.
- [36] J.S. Dai, X. Ding, Compliance analysis of a three-legged rigidly-connected platform device, *J. Mech. Des. Trans. ASME* 128 (4) (2006) 755–764.
- [37] W. Zhao, B. Li, Y. Hu, Stiffness analysis of a hybrid manipulator applied to a multi-dimensional vibration isolator, in: *IEEE Int. Conf. Mechatronics Autom. ICMA 2012*, 2012, pp. 1874–1879.
- [38] D. Wang, R. Fan, W.Y. Chen, Stiffness analysis of a hexaglide parallel loading mechanism, *Mech. Mach. Theory* 70 (2013) 454–473.
- [39] Y.G. Li, E.J. Zhang, Y.M. Song, Z.Y. Feng, Stiffness modeling and analysis of a Novel 4-DOF PKM for manufacturing large components, *Chinese J. Aeronaut* 26 (6) (2013) 1577–1585.
- [40] J. Zhang, Y. Zhao, J. Dai, Compliance Modeling and Analysis of a 3-RPS Parallel Kinematic Machine Module, *Chinese J. Mech. Eng. (English Ed.)* 27 (4) (2014) 703–713.
- [41] J. Zhang, Y. Zhao, Y. Jin, Kinetostatic-model-based stiffness analysis of exechon PKM, *Robot. Comput. Integr. Manuf.* 37 (2016) 208–220.
- [42] N.J. Ye, B. Hu, Stiffness modeling of some 4-DOF over-constrained parallel manipulators with various constrained wrench forms, *Mech. Mach. Theory* 172 (2022), 104821.
- [43] B. Hu, Y. Lu, Solving stiffness and deformation of a 3-UPU parallel manipulator with one translation and two rotations, *Robotica* 29 (6) (2011) 815–822.
- [44] S.A. Joshi, L. Tsai, Jacobian analysis of limited-DOF parallel manipulators, *ASME. J. Mech. Des.* 124 (2) (2002) 254–258.
- [45] J.W. Kim, K.W. Kim, H.S. Kim, J.H. Kyung, Stiffness analysis and design of a 3-DOF parallel robot with one constraining leg (ICCAS 2007), *ICCAS 2007 - Int. Conf. Control. Autom. Syst., (Iccas)* (2007) 2288–2293.
- [46] B. Hu, Kinematically identical manipulators for the exechon parallel manipulator and their comparison study, *Mech. Mach. Theory* 103 (9) (2016) 117–137.
- [47] L. Ching Sia, M. Dave, J.P. Sharma, T.A. McCarty, Stability analysis of muscular and skeletal system of human's leg segments (Thigh and Shank), *Int. J. Darshan Inst. Eng. Res. Emerg. Technol.* 9 (1) (2020) 1–8.
- [48] G.A. Pratt, M.M. Williamson, Series elastic actuators, *IEEE Int. Conf. Intell. Robot. Syst.* 1 (1995) 399–406.
- [49] E. Spyraeos-Papastavridis, J.S. Dai, Minimally model-based trajectory tracking and variable impedance control of flexible-joint robots, *IEEE Trans. Ind. Electron.* 68 (7) (2021) 6031–6041.
- [50] E. Spyraeos-Papastavridis, Z. Fu, J.S. Dai, Power-shaping model-based control with feedback deactivation for flexible-joint robot interaction, *IEEE Robot. Autom. Lett.* 7 (2) (2022) 4566–4573.
- [51] E. Spyraeos-Papastavridis, J.S. Dai, Stable flexible-joint floating-base robot balancing and locomotion via variable impedance control, *IEEE Trans. Ind. Electron.* (2022), 0046(c).
- [52] E. Spyraeos-Papastavridis, P.R.N. Childs, J.S. Dai, Passivity preservation for variable impedance control of compliant robots, *IEEE/ASME Trans. Mechatronics* 25 (5) (2020) 2342–2353.
- [53] E. Spyraeos-Papastavridis, J.S. Dai, P.R.N. Childs, N.G. Tsagarakis, Selective-compliance-based lagrange model and multilevel noncollocated feedback control of a humanoid robot, *J. Mech. Robot.* 10 (3) (2018).
- [54] P. Beillas, P.C. Begeman, K.H. Yang, A.I. King, P.J. Arnoux, H.S. Kang, K. Kayvantash, C. Brunet, C. Cavallero, P. Prasad, Lower limb: advanced FE model and new experimental data, *SAE Tech. Pap. (November)* (2001) 45.
- [55] B. Contini, Body segment parameters, part II, *Artif. Limbs* 16 (1) (1972) 1–19.
- [56] A.C. Satici, A. Erdogan, V. Patoglu, Design of a reconfigurable ankle rehabilitation robot and its use for the estimation of the ankle impedance, *IEEE Int. Conf. Rehabil. Robot.* (2009) 257–264.
- [57] C.G. Mattacola, M.K. Dwyer, Rehabilitation of the ankle after acute sprain or chronic instability, *J. Athl. Train.* 37 (4) (2002) 413–429.
- [58] B.S. El-Khasawneh, P.M. Ferreira, Computation of stiffness and stiffness bounds for parallel link manipulators, *Int. J. Mach. Tools Manuf.* 39 (2) (1999) 321–342.